ACS APPLIED ENERGY MATERIALS

www.acsaem.org Article

Reducing the Defect Formation Energy by Aliovalent Sn(+IV) and Isovalent P(+V) Substitution in Li_3SbS_4 Promotes Li^+ Transport

Bianca Helm, Kyra Strotmann, Thorben Böger, Bibek Samanta, Ananya Banik, Martin A. Lange, Yuheng Li, Cheng Li, Michael Ryan Hansen, Pieremanuele Canepa, and Wolfgang G. Zeier*

Cite This: https://doi.org/10.1021/acsaem.3c02652 Read Online

ACCESS | Metrics & More | Article Recommendations | Supporting Information

ABSTRACT: The search for highly conducting Li^+ solid electrolytes focuses on sulfide- and halide-based materials, where typically the strongly atomic disordered materials are the most promising. The atomic disorder corresponds to a flattened energy landscape having similar relative site energies for different Li^+ positions facilitating motion. In addition, the highly disordered Li^+ conductors have negligible defect formation energy as moving charges are readily available. This work investigates the isovalent $Li_3Sb_{1-x}P_xS_4$ ($0 \le x \le 0.5$) and the aliovalent $Li_{3+x}Sb_{1-x}Sn_xS_4$ ($0 \le x \le 0.2$) substitution series of thio-LISICON materials by using X-ray diffraction, high-resolution neutron diffraction, impedance spectroscopy, and defect calculations. The starting composition Li_3SbS_4 has a low ionic conductivity of $\sim 10^{-11}$ S·cm^{-1} and both substituents improve the ionic conductivity strongly by up to 4 orders of magnitude. On the one hand, in substituted Li_3SbS_4 structures, only minor structural changes are observed which cannot sufficiently explain the significant impact on the Li^+ conductivity. On the other hand, the Li^+ carrier density reveals a correlation to the activation energy and first-principles defect calculations, displaying significantly reduced defect formation energy upon substitution. Here, we show within two different substitution series that the defect formation energy plays a major role for ionic motion in this class of thio-LISICON materials.

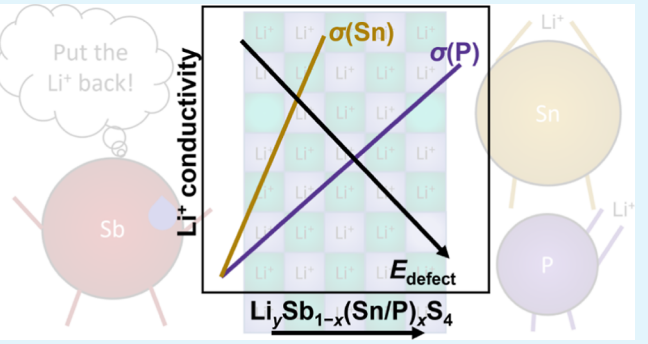

KEYWORDS: *thio-LISICON, solid electrolyte, defect formation energy, aliovalent substitution, isovalent substitution, impedance spectroscopy*

1. INTRODUCTION

All-solid-state batteries are a promising alternative to lithium-ion batteries.[1,2] Higher achievable energy densities due to employment of different electrode materials and a reduced flammability risk of the solid electrolyte are desirable properties.[2−4] Different material classes were probed for employment as solid electrolytes (requiring ionic conductivities in the mS-range) including argyrodite,[5−7] $Li_{10}GeP_2S_{12}$ (LGPS)[8] and LGPS-type,[9−12] rare-earth halide materials,[13−15] and thio-LISICONs.[16−18] The latter were the key in finding the superionic conductor $Li_{10}GeP_2S_{12}$.[8,19]

Thio-LISICONs offer a great variety of iso- and aliovalent substitutions and therefore represent an important playground for understanding Li^+ transport. Prominently, three polymorphs α, β, and γ are formed within this material class crystallizing in the space groups *Cmcm*, *Pnma*, and *Pmn*2_1, respectively.[20−22] The central nonlithium cation Li_yMS_4 determines the $(PnS_4)^{n-}$ ordering and therewith the polymorph, except for phosphorus where all three polymorphs are known.[4,21] For Li_3PS_4, the γ-polymorph exists at room temperature and the β-polymorph forms for temperatures above 543 K while the transition to the α-polymorph happens above 724 K.[21] The α-polymorph could recently be stabilized at room temperature by rapid heating from Li_3PS_4 glasses.[23] Forrester et al. were able to show by calculations that the $(PnS_4)^{n-}$ polyhedra carry out librational motions depending on the polymorph. The γ-polymorph exhibits no librational motion, while the α- and β-polymorphs perform different extents of librational motion.[24] The γ-polymorph is formed by pentavalent central cations $Li_3M^VS_4$ (M = P, Sb, As). γ-Li_3PS_4, Li_3AsS_4, and Li_3SbS_4 are reported to have low room-temperature conductivities of 3×10^{-7},[25] 1.31×10^{-5},[26] and 4.8×10^{-9} S·cm^{-1}, respectively.[27] A few iso- and aliovalent substitutions were performed for the γ-polymorph.[26,28] The substitution series $Li_3As_{1-x}Sb_xS_4$ ($0 \le x \le 1$) can be prepared as phase pure and an increase in unit cell volume can be observed for higher Sb contents. The best ionic conductivity

Received: October 20, 2023
Revised: January 21, 2024
Accepted: February 17, 2024

https://doi.org/10.1021/acsaem.3c02652
ACS Appl. Energy Mater. XXXX, XXX, XXX−XXX

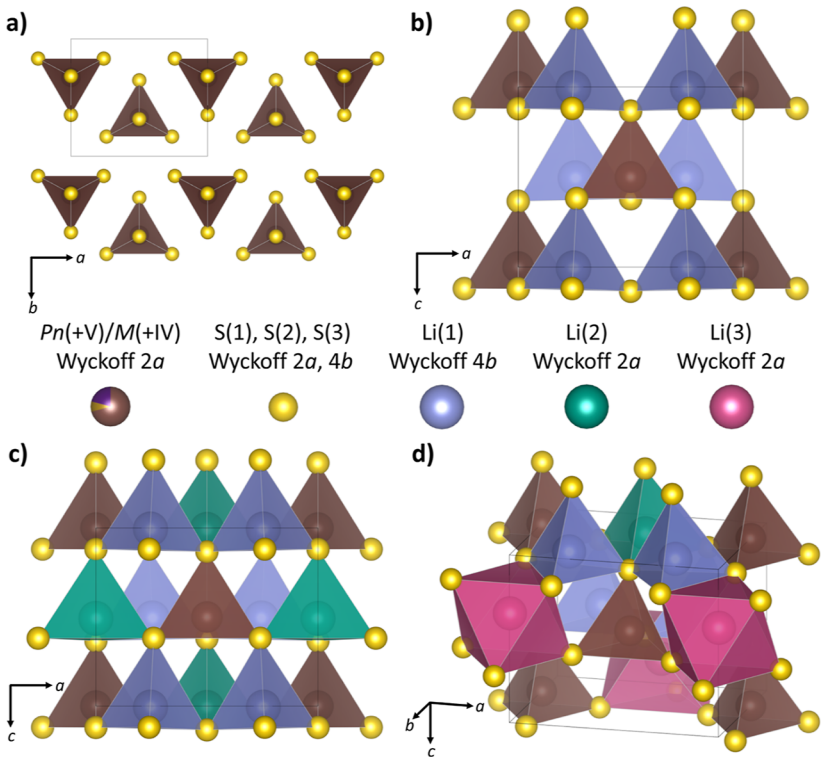

Figure 1. (a) Display of the typical $(PnS_4)^{3-}$ arrangement, where all apexes of the tetrahedra point in the *c*-direction, of the γ-Li_3PS_4 polymorph. (b) $(PnS_4)^{3-}$ tetrahedra are corner-sharing to the Li(1) site. (c) Second lithium site Li(2) is corner-sharing to the $(PnS_4)^{3-}$ tetrahedra and to Li(1) site. This corner-sharing network depicts the Li_3SbS_4 and $Li_3Sb_{1-x}P_xS_4$ structure. (d) For the $Li_{3+x}Sb_{1-x}Sn_xS_4$ substitution series, the additional Li^+ are placed onto the octahedral Li(3) interstitial site. Li(3) is edge-and face-sharing to Li(1) and Li(2) and just edge-sharing to $(PnS_4)^{3-}$ tetrahedra.

for the unsubstituted material was 3.2×10^{-5} S·cm^{-1}.[28] In the $Li_{3+x}As_{1-x}Ge_xS_4$ ($0 \le x \le 0.5$) substitution series, the ionic conductivity increases from aforesaid 1.31×10^{-5} S·cm^{-1} to 1.12×10^{-3} S·cm^{-1} for $Li_{3.334}As_{0.666}Ge_{0.334}S_4$ while keeping the γ-polymorph ($Pmn2_1$).[26] Additionally, Al-Qawasmeh and Holzwarth stated that in the computed substitution series $Li_{3+x}As_{1-x}Ge_xS_4$, germanium reduces the migration energy for interstitial Li ions and vacancies.[29] The $Li_{3-3x}Cu_{3x}SbS_4$ ($0 \le x \le 1$) substitution series did not affect the ionic conductivity as long as the compounds crystallized in the orthorhombic space group.[28]

The crystal structure of the γ-polymorph consists of one tetrahedral pnictide site $(PnS_4)^{n-}$, having all tetrahedral apexes pointing in the *c*-direction (Figure 1a), and two tetrahedral Li^+ sites, Li(1) (Wyckoff 4*b*) and Li(2) (Wyckoff 2*a*) (Figure 1b,c). All tetrahedral sites together form a corner-sharing framework.[21,27,29] The Li_3SbS_4 and the $Li_3Sb_{1-x}P_xS_4$ substitution series crystallize in the same structure (Figure 1c). The introduction of excess Li^+ into the structure, e.g., for $Li_{3+x}Sb_{1-x}Sn_xS_4$ substitution series, results in the occupation of an additional octahedral lattice site (Figure 1d), in accordance with the computationally proposed octahedral Li^+ position for $Li_{3+x}As_{1-x}Ge_xS_4$.[29]

Especially, the $Li_{3+x}As_{1-x}Ge_xS_4$ substitution series emphasizes that good conductivities are achievable within the γ-polymorph ($Pmn2_1$). However, the understanding of the Li^+ migration mechanism is limited. A migration mechanism involving a Li^+ interstitial site is expected to have the lowest activation barrier for this structure type.[29,30] In order to achieve a better understanding of this material class, the substitution series $Li_3Sb_{1-x}P_xS_4$ ($0 \le x \le 0.5$) and $Li_{3+x}Sb_{1-x}Sn_xS_4$ ($0 \le x \le 0.2$) are chosen to assess the impact of both, an aliovalent and an isovalent substituent on the Li_3SbS_4 structure. A combination of X-ray and neutron diffraction, impedance spectroscopy, and first-principles defect calculations shows the impact of several descriptors: (i) the Li^+ carrier density, (ii) the large size difference of Sb(+V) and P(+V), and (iii) the possibly changing Li^+ substructure[16,31] with the potential influence on ionic transport. The crystal structure of the solid electrolyte is impacted differently by P(+V) and Sn(+IV) substitution. In particular, the solubility limit of P(+V) is much higher in Li_3SbS_4 compared to Sn(+IV) resulting in less pronounced geometrical changes in $Li_{3+x}Sb_{1-x}Sn_xS_4$ in contrast to $Li_3Sb_{1-x}P_xS_4$ substitution series. However, at the respective maximum solubility limits the ionic conductivities are comparable and both series can achieve increased ion transport properties of up to 4 orders of magnitude. The activation energy shows a correlation to the Li^+ carrier density in both substitution series. Together with the strong changes in ionic transport, this study suggests that the enhanced Li^+ motion is related to the changing defect formation energies. Overall, this work provides an overview and direct comparison of the impact of an aliovalent and an isovalent substitution in the thio-LISICON Li_3SbS_4.

2. EXPERIMENTAL SECTION

2.1. Synthesis. The syntheses were performed completely under an inert atmosphere. Both substitution series $Li_3Sb_{1-x}P_xS_4$ ($0 \le x \le 0.5$) and $Li_{3+x}Sb_{1-x}Sn_xS_4$ ($0 \le x \le 0.20$) were prepared mechanochemically followed by an annealing step. The starting materials Li_2S (Alfa Aesar, 99.9%), Sb (ChemPur, 99.999%), S (Acros Organics, 99.999%), and P_2S_5 (Sigma-Aldrich, 99%), or Sn (ChemPur, 99.7%) were used in stoichiometric amounts with a slight excess of 4 mol % Li_2S. The mixtures were homogenized in an

https://doi.org/10.1021/acsaem.3c02652
ACS Appl. Energy Mater. XXXX, XXX, XXX−XXX

agate mortar before transferring the powders into the ball mill cups. The powder-to-milling ratio was 1:30 with a milling media size of 5 mm. The samples were mechanochemically milled for 72 cycles at 360 rpm. One cycle consisted of 15 min of milling followed by a 5 min break. Subsequently, the powders were pressed into pellets and transferred into a carbon-coated and predried quartz ampule (800 °C for 2 h, dynamic vacuum). The ampules were sealed and the samples were annealed at 500 °C for 2 h in a tube furnace. Finally, samples were air-quenched and hand-ground for further characterization.

2.2. X-ray Diffraction. X-ray diffraction (XRD) measurements were carried out on a Stoe STADI P in Debye−Scherrer geometry with a Ge(111) monochromator and a Dectris MYTHEN2 1K detector, using Mo $K_{\alpha,1}$ radiation (λ = 0.7093 Å). The diffraction data were collected within a Q-range of 0.61−8.16 $Å^{-1}$. The samples were prepared and sealed in borosilicate glass capillaries (Hilgenberg, Ø = 0.5 mm) under an inert atmosphere.

2.3. Neutron Powder Diffraction. Neutron powder diffraction data of both substitution series containing the natural abundant mixture of Li isotopes were collected at the Oak Ridge spallation neutron source (Oak Ridge National Laboratory). The POWGEN automatic sample changer at POWGEN (BL-11A beamline) was used. The samples (∼3 g) were loaded under an inert atmosphere into a cylindrical vanadium can (Ø = 8 mm) which was sealed with a copper gasket to avoid air exposure during measurements. The data collection lasted 3.5 h per diffractogram in a high-resolution mode at room temperature using a single bank with a center wavelength of 1.5 Å.

2.4. Rietveld Analysis. Rietveld refinements were carried out on absorption-corrected neutron and laboratory XRD data using the TOPAS-Academic V6 software package.[32] For all substitutions, refinements of the neutron and laboratory X-ray data were performed. The structural parameters for Li_3SbS_4 from Kimura et al. were used as a starting model for the refinement.[27] A convolution of pseudo-Voigt and GSAS back-to-back exponential functions was used to fit the profile shape of the neutron diffraction data.[33] The profile shape of the laboratory XRD data was fit with a Thompson−Cox−Hastings pseudo-Voigt function.[34] Initially the (1) background, (2) scale factors of main and side phases, (3) lattice parameter, and (4) the peak shape were refined. After a good fit of the profile was achieved, the (5) atomic coordinates, (6) occupancies, and (7) isotropic thermal displacements parameters were refined.

2.5. $Li_3Sb_{1-x}P_xS_4$. The refinements were carried out under the assumption that phosphorus replaces antimony on its site. Thus, the atomic coordinates and isotropic thermal displacement were constrained to be the same for phosphorus and antimony. Furthermore, the combined occupancy was constrained to unity. Additional Li^+ interstitial sites were probed for Li^+ occupancy, however, no meaningful values were obtained for occupancies and isotropic thermal displacements. Therefore, the occupancy of the initial lithium sites Li(1) and Li(2) was kept at unity. Finally, all parameters were refined together. The variables regarding Li^+ were globally refined from the neutron diffraction data, while the P/Sb-ratio was refined globally from the X-ray data. All residual variables were refined from both data sets.

2.6. $Li_{3+x}Sb_{1-x}Sn_xS_4$. The refinements were performed by replacing antimony with tin, therefore, the atomic coordinate and isotropic thermal displacement were constrained to be the same. The combined occupancy of antimony and tin was constrained to unity. Since the aliovalent substitution introduces more Li^+ into the structure, new Li^+ sites were explored. However, Li^+ could not be stabilized on any interstitial site. This is likely related to the observed asymmetric reflection shape of the (110) and (011) reflections with varying tin content (Figure S1). For the neutron measurement, several samples had to be synthesized to achieve about 3 g of the total sample amount, being necessary for the data acquisition and the reason for this left-side tailing. To keep the electroneutrality of the structure, additional Li^+ was placed on the octahedral interstitial Li(3).[29] This decision is based on the computed alloy of Li_3AsS_4−Li_4GeS_4 which crystallizes in the same space group and introduces additional Li^+ into the crystal structure as well. Al-Qawasmeh et al. found that germanium stabilizes Li^+ on the additional site named "x", which resembles the Li(3) site used here.[29] Additionally, ^{6}Li magic-angle spinning (MAS) nuclear magnetic resonance (NMR) spectra were collected for $Li_{3.2}Sn_{0.8}Sb_{0.2}S_4$ confirming the interstitial Li(3) site (Figure S7). Moreover, for the observed Li_4SnS_4 side phase, ^{6}Li MAS NMR measurements were conducted as well to exclude or pinpoint contribution to the peaks in the spectrum of $Li_{3.2}Sn_{0.8}Sb_{0.2}S_4$. The Li^+ occupancies of Li(1), Li(2), and Li(3) are freely refined within the Li^+ constraint; however, the occupancy of Li(1) and Li(2) always remained at unity for all samples. Thus, all additional Li^+ were placed onto the Li(3) site. It was possible to refine the atomic coordinates and the isotropic thermal displacement of Li(3) in the refinement process; however, it was not possible to open every variable concerning Li(3) at the end of the refinement for higher tin contents [x(Sn) ≥ 0.15]. All other parameters were refined together. The variables related to Li^+ and the Sb/Sn-ratio were refined globally from neutron diffraction data. For all other parameters, the X-ray and neutron diffraction data set were both taken into account.

VESTA was used to calculate polyhedral volumes.[35] The estimated standard deviation is shown as error bars in all data, except for the polyhedral volume uncertainties, which were calculated from bonds' distance uncertainties. For simplicity, the formula of a perfect tetrahedron or octahedron was used. All structural tables, crystallographic information files (CIFs), and used constraints (Figures S2−S4 and Tables S1−S12) can be found in the Supporting Information.

2.7. Potentiostatic Electrochemical Impedance Spectroscopy. Ionic conductivities were measured with AC impedance spectroscopy in a pouch cell setup. 150−200 mg of powders was isostatically pressed. The bore diameter was 32 mm. The pellets were pressed for 40 min at 3.98 kbar. The relative pellet densities are 74−83% for $Li_{3+x}Sb_{1-x}Sn_xS_4$ and 80−88% for $Li_3Sb_{1-x}P_xS_4$ (Table S13). Afterward, a circular gold layer was sputtered onto both sides of the pellet with a sputtering current of 30 mA for 300 s. The pressure in the sputter chamber was 0.05 mbar and the diameter of the circular gold layer was 8 mm. Lastly, the pellets were contacted to aluminum current collectors and sealed in pouch bags. The impedance measurements were carried out with a SP300 impedance analyzer (Biologic) in a temperature range of 298−333 K and in a frequency range of 7 MHz to 100 mHz with an amplitude of 30 mV. The impedance spectra were analyzed with RelaxIS (rhd instruments) software.

2.8. Defect Formation Energy Calculations. Using density functional theory (DFT), as implemented in the Vienna ab initio simulation package, the geometries of Li_3PS_4, Li_3SbS_4, and Li_4SnS_4, as well as all potentially stable phases of the ternary phase diagrams were relaxed (coordinates + shape + volume).[36−38] The Perdew−Burke−Ernzerhof[39] functional within the generalized gradient approximation (GGA), an energy convergence criterion of 10^{-6} eV, a force cutoff of 10^{-3} eV/Å for the unit cell relaxation and 10^{-2} eV/Å for the other compounds of the phase diagram relaxations, and a Γ-centered k-point mesh of at least 7 points per $Å^{-1}$ were used. Wave functions were expanded as plane waves with an energy cutoff of 650 eV whereas core electrons were treated with the projector-augmented-wave potentials.[40] Input geometries and postprocessing were obtained with the pyCDT-package.[41] A 2 × 2 × 2 supercell was used for the defect calculations with an energy convergence criterion of 10^{-4} eV, a force convergence criterion of 10^{-2} eV/Å, and a Γ-centered k-point mesh of at least 4 points per $Å^{-1}$. To avoid the common underestimation of band gaps by semilocal GGA functionals, the HSE06 hybrid functional was used.[42] Defect formation energies were corrected utilizing the methodology outlined by Freysoldt.[43]

2.9. Nuclear Magnetic Resonance Spectroscopy. Solid-state ^{6}Li MAS NMR spectra were recorded using a Bruker DSX 500 spectrometer equipped with a wide bore magnet (B_0 = 11.7 T, ν_L = 73.6 MHz), with a 4 mm Bruker MAS probe. For Li_4SnS_4, single-pulse excitation experiment was performed using a $\pi/2$-pulse length of 7 μs at 100 W and a recycle delay of 5s. For $Li_{3.2}Sb_{0.8}Sn_{0.2}S_4$, a quantitative spectrum was obtained with a short flip angle of $\pi/12$ (1.167 μs at 100 W) and a recycle delay of 10 s to ensure complete relaxation of all the components present. A spinning frequency of 12.5

https://doi.org/10.1021/acsaem.3c02652
ACS Appl. Energy Mater. XXXX, XXX, XXX−XXX

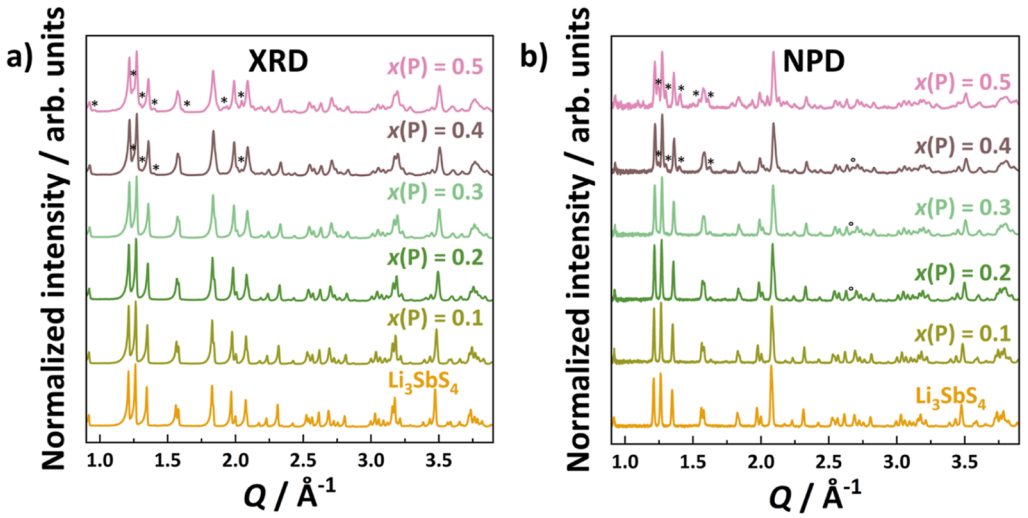

Figure 2. Stacked (a) X-ray and (b) neutron diffractograms of the substitution series $Li_3Sb_{1-x}P_xS_4$. For nominal substitution degrees larger than x(P) = 0.4, side phases are observable and can be assigned to γ- and β-Li_3PS_4 hinting at a solubility limit of P(+V) in Li_3SbS_4. The Li_3PS_4 side phases are marked with *. Due to overlapping reflections, no distinction is made between the γ- and β-phase for simplicity, and just the most intense reflections of the Li_3PS_4 polymorphs are marked. Additionally, an unknown side-phase reflection (marked with °) can be seen in the neutron diffraction data, which is much less pronounced in the XRD patterns.

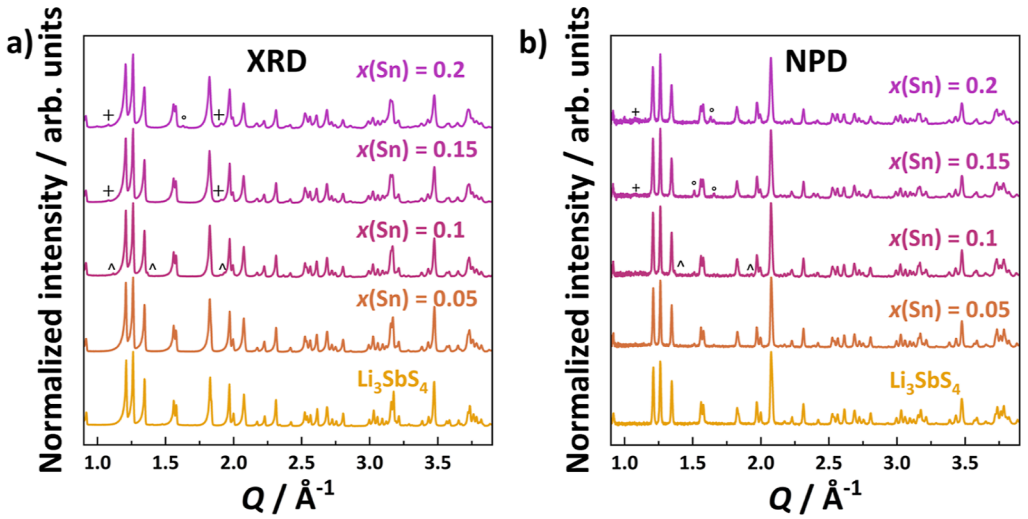

Figure 3. Stacked (a) X-ray and (b) neutron diffraction plots of $Li_{3+x}Sb_{1-x}Sn_xS_4$ are shown up to x(Sn) = 0.2. The $Li_{3.10}Sb_{0.90}Sn_{0.10}S_4$ sample has Li_3SbS_3 marked with ∧ as an impurity. In the samples $Li_{3.15}Sb_{0.85}Sn_{0.15}S_4$ and $Li_{3.20}Sb_{0.80}Sn_{0.20}S_4$, Li_4SnS_4 reflections are marked by + as impurities indicating a solubility limit. Reflections of an unknown side phase (marked with °) are found in this substitution series.

kHz was used for all samples. Fitting and deconvolution were performed using ssNake v1.4 software.

All samples were packed into 4 mm Zirconia rotors (inside glovebox; H_2O < 0.5 ppm, O_2 < 0.5 ppm) with single Vespel top cap and Teflon spacers to minimize moisture exposure during experiments. Magic-angle calibration was performed using the spinning sidebands of the ^{23}Na resonance from solid $NaNO_3$. The ^6Li chemical shift was referenced to the most intense signal of ^6Li-enriched solid CH_3COOLi at 0 ppm.

3. RESULTS AND DISCUSSION

3.1. Synthesis and Solubility Limits. The substitution series $Li_{3+x}Sb_{1-x}Sn_xS_4$ and $Li_3Sb_{1-x}P_xS_4$ were synthesized by the mechanochemical method with subsequent annealing and air-quenching. The phase purity is probed with XRD. Additional neutron diffraction data are collected to investigate the Li^+ substructure. The X-ray and neutron diffraction patterns of $Li_3Sb_{1-x}P_xS_4$ are shown in Figure 2.

The P(+V) substitution of Li_3SbS_4 crystallizes in the γ-polymorph over the investigated substitution range (Figure 2a).[21] The first additional reflections are observed for nominal composition larger than x(P) = 0.4 belonging to the γ- and β-Li_3PS_4 polymorphs. In particular for $Li_3Sb_{0.6}P_{0.4}S_4$, γ-Li_3PS_4 [9.4(2) wt %] forms as a side phase, and for the $Li_3Sb_{0.5}P_{0.5}S_4$, a mixture of γ-Li_3PS_4 [10.4(2) wt %] and β-Li_3PS_4 [10.2(2) wt %] is observed. For simplicity, the γ- and β-Li_3PS_4 polymorph reflections are marked with the same symbols due to overlapping reflections from the high degree of similarity of the crystal structure because of similar lattice plane spacings. The formation of the Li_3PS_4 structures hints at a solubility limit of around 30 at. % of P(+V) on the Sb(+V) site. Furthermore, the neutron diffraction patterns reveal an unknown side phase (Figure 2b), which is much less intense in the XRD pattern. Thus, the reflection must belong to a composition with elements that exhibit weak X-ray scattering

https://doi.org/10.1021/acsaem.3c02652
ACS Appl. Energy Mater. XXXX, XXX, XXX−XXX

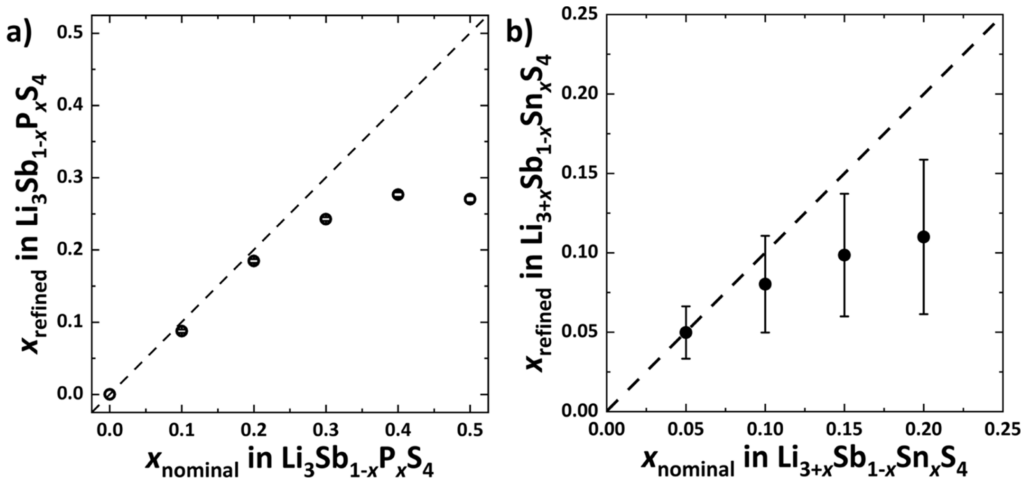

Figure 4. Trends in solubility of (a) P(+V) and (b) Sn(+IV) in Li_3SbS_4. A maximum content of 27 at. % of P(+V) on the Sb(1) site is found, while for Sn(+IV) a maximum of 11 at. % is found. The dashed lines indicate the perfect solubility.

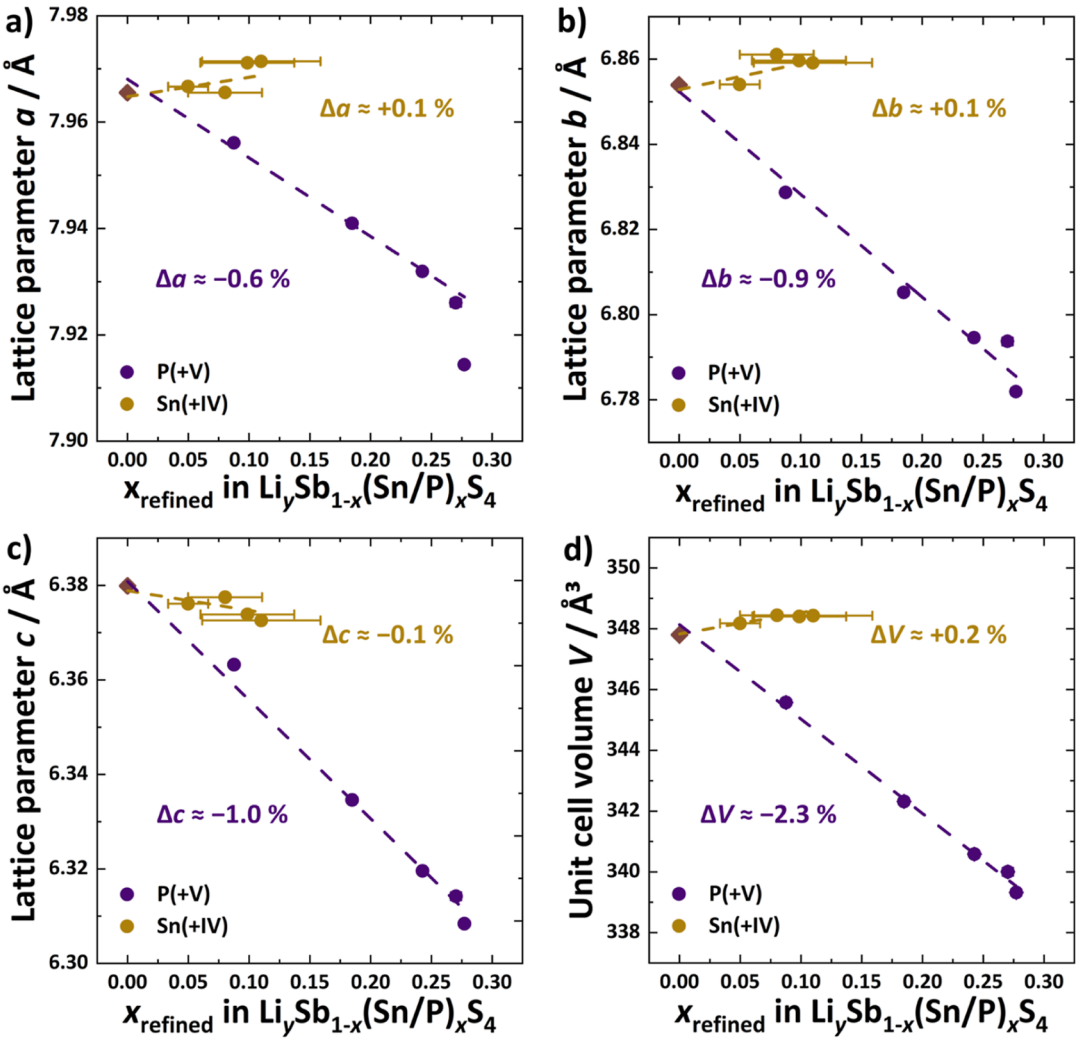

Figure 5. (a) P(+V) substitution decreases lattice parameter a while the lattice parameter a increases for Sn(+IV) substitution. (b) Lattice parameter b increases for the Sn(+IV) substitution and decreases for the P(+V) substitution. (c) Lattice parameter c decreases for both substitution series. (d) P(+V) substitution shrinks the unit cell volume while the Sn(+IV) substitution enlarges the unit cell slightly. The *y*-errors are within the magnitude of the symbols for every plot. The dashed lines are guides to the eye.

form factors, but it could not be assigned to any specific phase as just one impurity reflection is observed.

The aliovalent Sn(+IV) substitution series is synthesized up to a nominal content of 20 at. % Sn(+IV) on the Sb(+V) site

https://doi.org/10.1021/acsaem.3c02652
ACS Appl. Energy Mater. XXXX, XXX, XXX−XXX

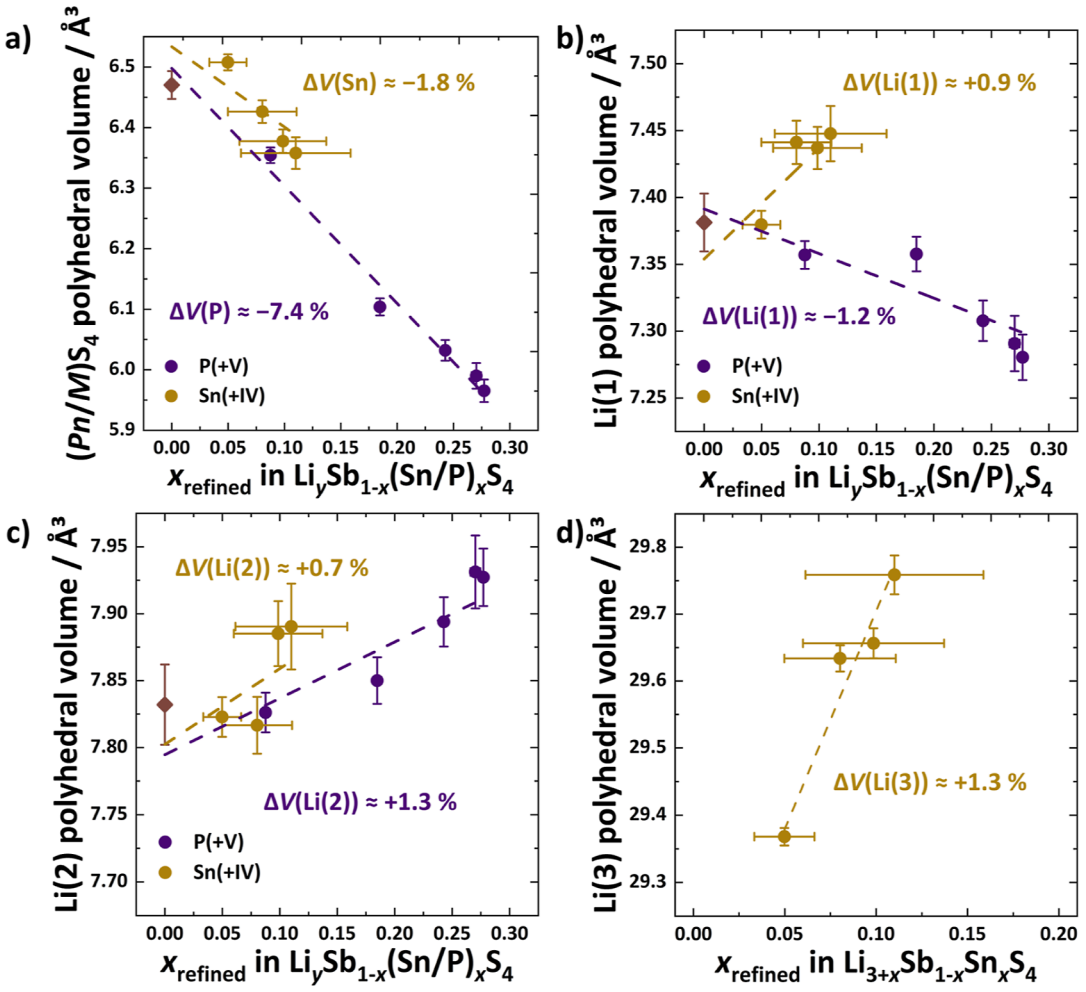

Figure 6. (a) Display of the decrease in $(Pn/M)S_4$ polyhedron volume for P(+V) substitution and Sn(+IV) substitution in Li_3SbS_4. (b) Li(1) tetrahedron volume increases for Sn(+IV) substitution and decreases for the P(+V) substitution. (c) Li(2) polyhedron volume increases for both substitution series. (d) Li(3) octahedron volume increases for higher Sn(+IV) content. The dashed lines are guides to the eye.

(Figure 3). Similar to the P(+V) substitution, the Sn(+IV) substitution crystallizes in the γ-polymorph over the investigated substitution range (Figure 3a). For nominal contents of more than x(Sn) = 10 at. %, side phases can be observed. The $Li_{3.10}Sb_{0.90}Sn_{0.10}S_4$ samples contain Li_3SbS_3 (2.84(5) wt %) as a side phase (Figure 3a), where loss of sulfur during the reaction can be the reason for the development of this impurity. The diffraction patterns of the two highest tin content phases of 15 and 20 at. % indicate the presence of Li_4SnS_4 as the secondary phase, containing 4.8(1) and 9.8(1) wt %, respectively. This implies a solubility limit of 10 at. % of Sn(+IV) in Li_3SbS_4. Some additional reflections can be observed in neutron diffraction and XRD patterns which cannot be assigned to any specific phase. The solubility limits, which are estimated from the diffraction patterns, are in accordance with the Rietveld refinement results (Figure 4).

Besides the large radius difference of 0.33 Å,[44,45] P(+V) can be incorporated up to 27(1) at. % on the Sb(+V) site, based on the Rietveld refinements. The radius similarity of Sn(+IV) (0.55 Å)[44] and Sb(+V) (0.50 Å)[45] in tetrahedral coordination would suggest a higher solubility limit than P(+V) but just up to 11(4) at. % of Sn(+IV) can be incorporated into the Li_3SbS_4 structure. The lower solubility limit of Sn(+IV) compared to P(+V) could stem from the preference of Sn(+IV) to form Li_4SnS_4 in the β-polymorph.[16] From now on, the unit cell parameters and polyhedra volumes are displayed against the refined P(+V)/Sn(+IV) content to depict reality more accurately.

3.2. Unit Cell and Polyhedra Changes. By evaluation of the X-ray and neutron diffractograms with Rietveld refinements, the geometrical adaptions of the Li_3SbS_4 structure upon P(+V) and Sn(+IV) substitution are monitored. First, the lattice parameter a, b, and c as well as the unit cell volume V are determined (Figure 5) and changes are given are as percentage values to better assess the magnitude of total structural changes.

The P(+V) substitution in Li_3SbS_4 leads to a decrease of all lattice parameters, where a, b, and c reduce about 0.6, 0.9, and 1.0%, respectively. In contrast, the introduction of Sn(+IV) in Li_3SbS_4 leads to a slight increase in lattice parameter a (0.1%) and lattice parameter b (0.1%) while lattice parameter c is decreased (0.1%). The overall unit cell volume shrinks for the P(+V) substitution by about 2.3% and enlarges for the Sn(+IV) substitution by about 0.2% (Figure 5d). However, keep in mind that the smaller changes of Sn(+IV) compared to P(+V) can be reasoned by the lower solubility of Sn(+IV) in the Li_3SbS_4 structure. In addition, the similar radius size of Sn(+IV) and Sb(+V) may also diminish the extent of structural changes. The $(Sb_{1-x}P_xS_4)^{3-}$ tetrahedron volume shrinks by about 7.4% upon P(+V) incorporation (Figure 6a), while the

https://doi.org/10.1021/acsaem.3c02652
ACS Appl. Energy Mater. XXXX, XXX, XXX−XXX

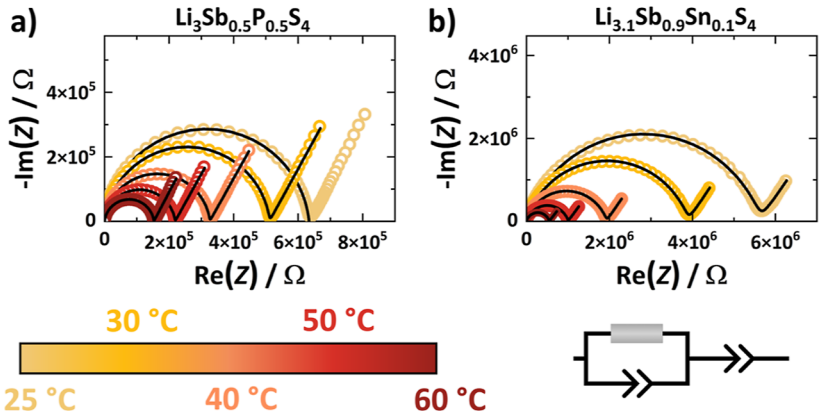

Figure 7. Exemplary temperature-dependent impedance spectra of (a) nominal composition $Li_3Sb_{0.5}P_{0.5}S_4$ and (b) nominal composition $Li_{3.1}Sb_{0.9}Sn_{0.1}S_4$. The solid lines represent actual fits. Nonfitted data points were excluded with the Kramers−Kronig relationship.

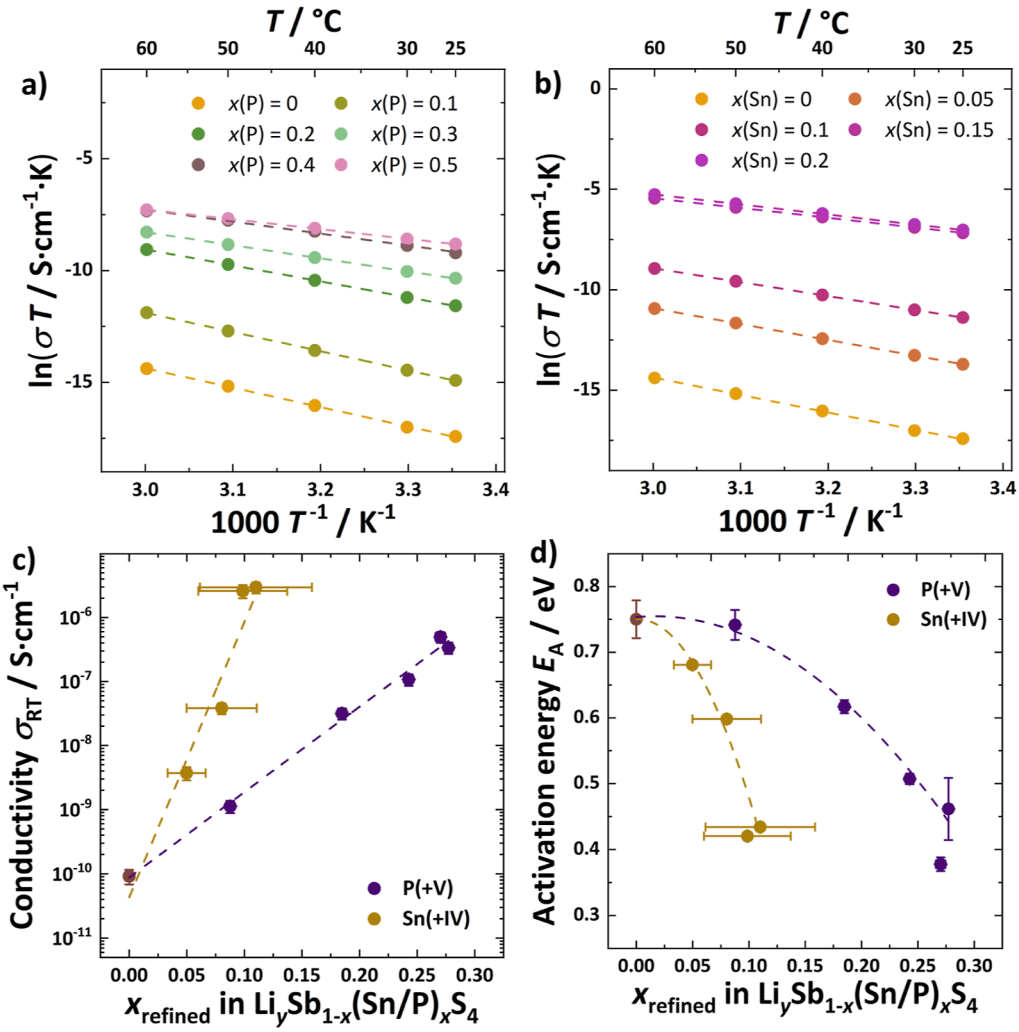

Figure 8. Arrhenius plots of the substitution series (a) $Li_3Sb_{1-x}P_xS_4$ and (b) $Li_{3+x}Sb_{1-x}Sn_xS_4$ showing the expected linear behavior in the investigated temperature range. The description in (a,b) refers to nominal compositions. (c) Room-temperature conductivity σ_{RT} of both substitution series shows a linear increase with higher substituent content in the crystal structure. (d) Activation energy E_A decreases with higher P(+V) and Sn(+IV) content to roughly the same value for the highest substitution degree. The dashed lines in (a,b) are actual fits, while the dashed lines in (c),d) are guides to the eye.

$(Sb_{1-x}Sn_xS_4)^{(3-x)-}$ tetrahedron volume is reduced by about 1.8% upon Sn(+IV) introduction. For the P(+V) substitution, a decrease in tetrahedron volume is expected, however, the decreasing $(Sb_{1-x}Sn_xS_4)^{(3-x)-}$ volume seems rather unexpected. In particular, Sn(+IV) (r = 0.55 Å)[44] and Sb(+V) (r = 0.50 Å)[45] in tetrahedral coordination are similar in size and Sn(+IV) has a lower valence than Sb(+V). On the basis of a purely Coulombic argument, the electrostatic attraction

https://doi.org/10.1021/acsaem.3c02652
ACS Appl. Energy Mater. XXXX, XXX, XXX−XXX

between Sn−S should be lower than Sb−S, resulting in longer bonds. Additionally, the magnitude of the wavenumbers of the $(SnS_4)^{4-}$ and $(SbS_4)^{3-}$ stretching modes in Raman gives insights about the bond strength as the force constant can be estimated.[46] The symmetric stretching mode of $(SnS_4)^{4-}$ and $(SbS_4)^{3-}$ is expected at ∼345 and ∼360 cm^{-1}, respectively.[27,46−48] A smaller wavenumber corresponds to a smaller force constant,[46] hence the Sn−S bond should also be longer than Sb−S in terms of covalent bonding. Therefore, the reduction of $(Sb_{1-x}Sn_xS_4)^{(3-x)-}$ volume might be rather related to the additional number of Li^+ in the structure.

For the $Li_3Sb_{1-x}P_xS_4$ substitution series, the Li(1) tetrahedron volume decreases by about 1.2% and the Li(2) tetrahedron volume increases by about 1.3% (Figure 6b,c). The $Li_{3+x}Sb_{1-x}Sn_xS_4$ substitution series depicts an expansion in Li(1) (0.9%) and in Li(2) (0.7%) tetrahedron volume (Figure 6b,c). Additionally, the Li(3) octahedron enlarges with higher Sn(+IV) contents (Figure 6d). The very minor unit cell expansion for the Sn(+IV) substitution seems to be driven by the Li^+ substructure, as the volume of $(Sb_{1-x}Sn_xS_4)^{(3-x)-}$ tetrahedron, the only nonlithium cation site, reduces and all occupied lithium polyhedra are expanding in size. Furthermore, the unit cell shrinkage of the P(+V) substitution shows mixed volume changes for the Li^+ polyhedra, which prevents us to identify the main driving factor of the overall unit cell volume reduction.

3.3. Ionic Transport. Changes in ionic transport were probed with temperature-dependent potentiostatic impedance spectroscopy. Exemplary impedance responses and their fits are shown in Figure 7. The Nyquist plots of the other compositions can be found in Supporting Information (Figures S5 and S6).

The compositions of Li_3SbS_4 and lower substitution degrees are highly resistive, hence the monitored temperature range is 25−60 °C. At lower temperatures, the semicircles cannot be as nicely resolved as the semicircles at room temperature (Figures S5 and S6). The impedance spectra are fit with equivalent circuits depending on the observed features. For the more resistive samples, a resistor in parallel to a constant-phase element (CPE) is used because just a semicircle is observable. The better-conducting samples exhibit a semicircle and the blocking tail of the gold electrodes; thus, the impedance spectra are fit with a resistor in parallel to a CPE in series with a CPE (Figure 7). As it is indicative in Figure 7a, the impedance spectra of $Li_{3+x}Sb_{1-x}Sn_xS_4$ show suppressed semicircles, which is also reflected in the α-values ranging from 0.82 to 0.95 and capacitances ranging between 8×10^{-11} and 1×10^{-10} F. The substitution series $Li_3Sb_{1-x}P_xS_4$ exhibits α-values of 0.85 to 0.93 and lower capacitances between 3×10^{-11} and 8×10^{-11} F. The nonideal α-values and capacitances for both substitution series hint at a mixture of in-grain diffusion and transport across grain boundaries.[49,50] Thus, the reported values correspond to total conductivity values. Both substitution series exhibit Arrhenius-like behavior over the monitored temperature range (Figure 8a,b).

The room-temperature conductivity of Li_3SbS_4 is determined to be $9.2(7) \times 10^{-11}$ S·cm^{-1} (Figure 8), which is nearly 2 orders of magnitude lower than the value of 4.8×10^{-9} S·cm^{-1} (25 °C) reported by Kimura et al.[27] In addition, Matsuda et al. reported an ionic conductivity of Li_3SbS_4 synthesized by an ion-exchange process of 8.5×10^{-8} S·cm^{-1} (50 °C), being 2 orders of magnitude higher than the herein-found conductivity at 50 °C of Li_3SbS_4.[51] Furthermore, Huber et al. report an ionic conductivity of 3.2×10^{-7} S·cm^{-1} (267 °C) for Li_3SbS_4 synthesized by a solid-state synthesis.[52] Hence, the synthesis procedure most likely influences the resulting ionic conductivity.[53,54]

The room-temperature conductivity increases for both substituents (Figure 8c). However, the Sn(+IV) substitution leads to a 3-fold faster increase in ionic conductivity than the P(+V) substitution. The highest obtained room-temperature ionic conductivity values are $2.9(2) \times 10^{-6}$ S·cm^{-1} for $Li_{3.2}Sb_{0.8}Sn_{0.2}S_4$ and $4.9(9) \times 10^{-7}$ S·cm^{-1} for $Li_3Sb_{0.5}P_{0.5}S_4$, which are 5 and 4 orders of magnitude higher than the conductivity of Li_3SbS_4, respectively. The activation energy reflects the opposite trend to the conductivity and is reduced to 0.37(1) and 0.43(1) eV for the P(+V) substitution and the Sn(+IV) substitution, respectively. In addition, the decrease in activation energy appears steeper for the Sn(+IV) than the P(+V) substitution, albeit both substitution series reach comparable activation energies for their highest substitution content. For higher substitution degrees, side phases with up to ∼20 wt % for P(+V) and up to ∼10 wt % for Sn(+IV) substitution form, possibly influencing the ionic conductivity. For the $Li_3Sb_{1-x}P_xS_4$, side phases, such as γ- and β-Li_3PS_4 are observed and for $Li_{3+x}Sb_{1-x}Sn_xS_4$, only Li_4SnS_4 is observed. β-Li_3PS_4 and γ-Li_3PS_4 have room-temperature conductivities of $\sim 9 \times 10^{-7}$ and 3×10^{-7} S·cm^{-1}, respectively.[21,25,55] The reported Li_4SnS_4 conductivity values range between 10^{-6} and 10^{-5} S·cm^{-1}.[56−59] Both solid solution series reached for their highest substitution degree of the ionic conductivity of the other end member, being Li_3PS_4 and Li_4SnS_4, thus no significant influence in the measured conductivity can be linked to the side phases in the investigated substitution range. Nevertheless, as soon as the phase mixture mainly consists of the side phases, namely Li_3PS_4 or Li_4SnS_4, these will impact the measured ionic conductivity directly. Overall, both substituents show a positive impact on Li^+ transport in the Li_3SbS_4 structure, where the aliovalent Sn(+IV) substitution enhances the Li^+ motion more efficiently than the isovalent P(+V) substitution.

3.4. Defect Formation Energies. To assess whether diffusion of Li^+ vacancies or Li^+ interstitials is dominating, defect formation energies were computed with DFT calculations. The formation of a variety of defects is possible in both the aliovalent $Li_{3+x}Sb_{1-x}Sn_xS_4$ and isovalent $Li_3Sb_{1-x}P_xS_4$ substitution series. However, which defects form, is preferably determined by the energy landscape, in particular the local bonding environment of a crystal system, which is influenced by the composition.[54]

Using the Kröger−Vink notation, a wide variety of defects is explored for each end member of the substitution series, e.g., Li_3SbS_4, Li_3PS_4, and Li_4SnS_4 such as Li^+ interstitials ($Li_i^{\bullet}$), Li^+ vacancies (V_{Li}'), sulfur vacancies ($V_S^{\bullet\bullet}$), and Sb(+V)/P(+V)/Sn(+IV) vacancies ($V_{Sb/P}''''''$ and V_{Sn}''''). To allow for a direct comparison, the defect formation energy calculations of Li_4SnS_4 were performed assuming that Li_4SnS_4 crystallizes in the γ-Li_3PS_4 structure, as Li_3SbS_4 does, and not in the experimentally found β-Li_3PS_4 modification.[16,59] The calculated defect formation energies with respect to the Fermi energy are shown in Figure 9.

The equilibrium Fermi level $E_{f,eq}$ decreases from Li_3SbS_4 (2.11 eV) over Li_3PS_4 (1.83 eV) to Li_4SnS_4 (1.38 eV), which is pinned by $Li_i^{\bullet}$ and V_{Li}'. At the $E_{f,eq}$ within all three end members, defects with lower charges, namely $Li_i^{\bullet}$ and V_{Li}', form easily than the higher charged defects, namely $V_S^{\bullet\bullet}$,

https://doi.org/10.1021/acsaem.3c02652
ACS Appl. Energy Mater. XXXX, XXX, XXX−XXX

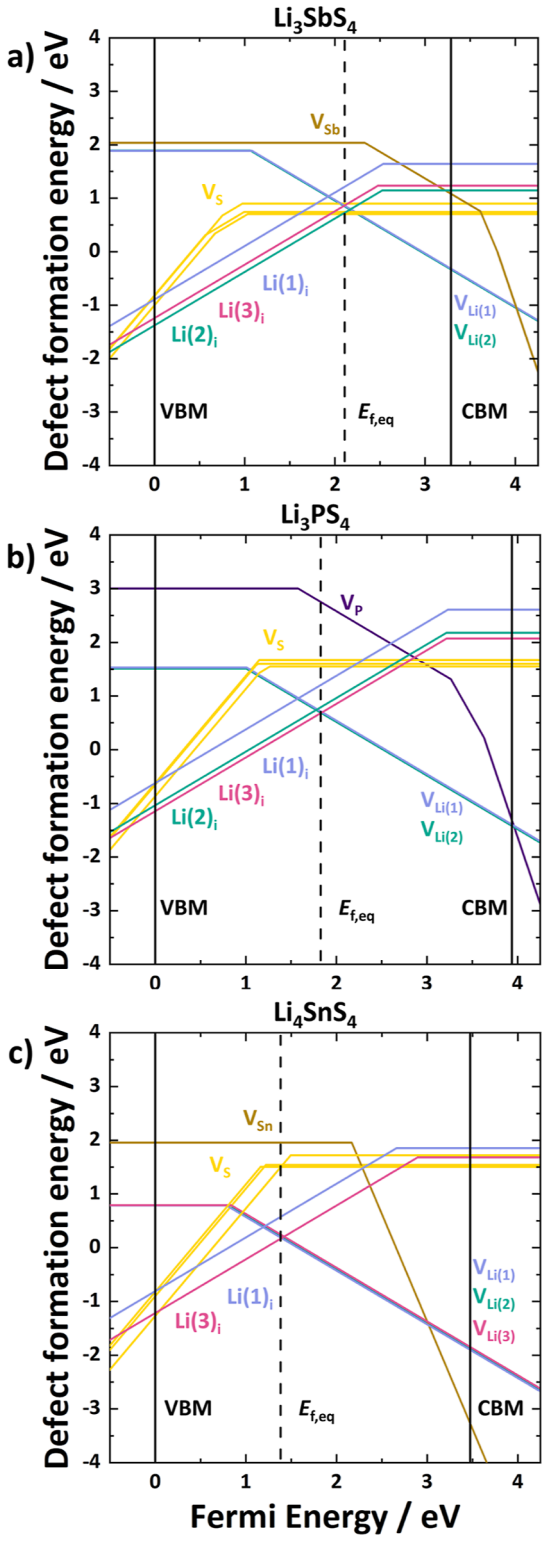

Figure 9. Defect formation energies of (a) Li_3SbS_4, (b) Li_3PS_4, and (c) Li_4SnS_4. The compositions are computed within the phase regions of Li_2S–Li_3SbS_4–S, Li_2S–Li_3PS_4–S, or Li_2S–Li_4SnS_4–S. The dashed line corresponds to the equilibrium Fermi level $E_{f,eq}$, where the charge sum of all the defects is zero, and the solid lines are the valence band maximum and conduction band minimum spanning the band gap of each bulk material.

$V_{Sb/P}''''''$, and V_{Sn}''''. The majority of charge carrier seems to be $Li_i^{\bullet}$ and V_{Li}' in every case when comparing the relative energetic position of $Li_i^{\bullet}$ and V_{Li}'. Furthermore, when changing the composition from Li_3SbS_4 to Li_3PS_4 or Li_4SnS_4, the formation energies of $Li_i^{\bullet}$ and V_{Li}' are reduced in both cases (Figure 10).

The vacancy formation on the Li^+ sites in Li_3SbS_4 requires an energy of about ~0.85 eV, while for γ-Li_3PS_4 and Li_4SnS_4 ~0.71 and ~0.21 eV are necessary, respectively (Figure 10a). In relative changes, the P(+V) and Sn(+IV) substitutions reduce the vacancy formation energy by 16 and 75%, respectively. In addition, the interstitial formation energy varies more within one compound than the formation energy of the vacancies (Figure 10b). The formation energy of interstitials ranges from 0.87 to 1.21 eV (Li_3SbS_4), 0.68 to 1.20 eV (γ-Li_3PS_4), and 0.17 to 0.58 eV (Li_4SnS_4). While in Li_4SnS_4 the Li^+ interstitial formation is significantly reduced, for γ-Li_3PS_4, it is similar to Li_3SbS_4. The smaller overall reduction in defect formation energy for γ-Li_3PS_4 compared to Li_4SnS_4 may be connected to the different inclines in conductivity improvement.

Lepley et al. reported relative formation energies of Li^+ vacancies and Li^+ interstitials for γ-Li_3PS_4. The relative vacancy formation energy of the Li(1) site is −0.04 eV with regard to the formation energy of a vacancy in the Li(2) site, while the herein-found vacancy formation energies differ about 0.03 eV. The interstitial formation energies are calculated relative to the $Li(3)_i^{\bullet}$ (set to 0 eV) and are 0.44 eV for $Li(1)_i^{\bullet}$ or 0 eV for $Li(2)_i^{\bullet}$.[60] Yang et al. determined the interstitial formation energies relative to $Li(3)_i^{\bullet}$ (set to 0 eV) finding 0.51 eV for $Li(1)_i^{\bullet}$ and 0.12 eV for $Li(2)_i^{\bullet}$.[30] Thus, the studies of Lepley et al.[60] and Yang et al.[30] are both agreeing that $Li(1)_i^{\bullet}$ has the highest defect formation energy of the interstitials, which is also found here. Moreover, the relative interstitial formation energies found herein are similar to Yang et al.,[30] being 0.52 eV ($Li(1)_i^{\bullet}$), 0.11 eV ($Li(2)_i^{\bullet}$), and 0 eV ($Li(3)_i^{\bullet}$), whereas the energies are referenced to $Li(3)_i^{\bullet}$.

Yang et al. determined different paths for Li^+ interstitial and vacancy diffusion in every unit cell direction for γ-Li_3PS_4, thereby finding that the direct hopping mechanism along the *c*-direction has the lowest energy barrier of 0.16 eV per ion jump. In addition, the vacancy diffusion barrier in the *c*-direction is determined to be 0.26 eV requiring almost double the energy than the easiest Li^+ interstitial mechanism in the same direction. Al-Qawasmeh et al. state that an interstitial or interstitialcy mechanisms for carrier migration might be more likely within the solid solution of $Li_{3+x}As_{1-x}Ge_xS_4$ (crystallizing also in the γ-polymorph) than a vacancy mechanism as the additional Li^+ already contribute to the interstitial population and some vacancy sites close to Ge sites are relatively unstable limiting the vacancy pathways. In addition, the introduction of tetravalent Ge adjusts the relative site energies of the Li^+ positions reducing the migration energy in solid solutions.[29] Hence, the substituents P(+V) and Sn(+IV) are expected to modify the energy landscape of the solid electrolyte, which in turn should facilitate Li^+ interstitial or vacancy transport.

In general, the computed defect formation energies are in line with the observed Li^+ transport as both substituents promote Li^+ motion. The 3-fold faster increase in Li^+ conductivity for $Li_{3+x}Sb_{1-x}Sn_xS_4$ compared to $Li_3Sb_{1-x}P_xS_4$ is reasoned with the stronger decrease in $Li_i^{\bullet}$ and V_{Li}' formation energies at the $E_{f,eq}$. The assumption has to be made that either all or a major part of the generated interstitials and vacancies contribute to the ionic transport. Looking at the Li^+ carrier density, being calculated as the refined number of Li^+ divided

https://doi.org/10.1021/acsaem.3c02652
ACS Appl. Energy Mater. XXXX, XXX, XXX−XXX

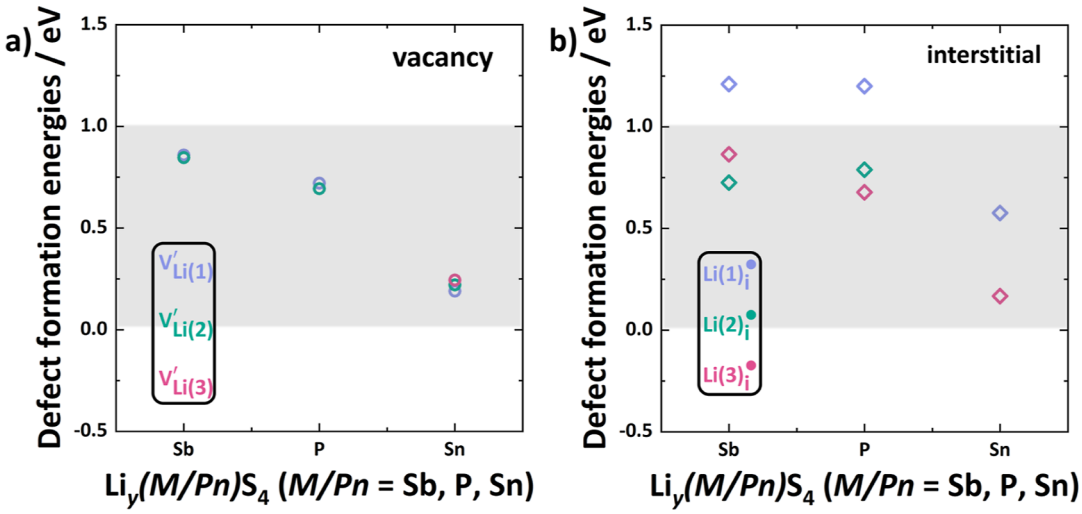

Figure 10. Comparison of the (a) V_{Li}' and (b) $Li_i^{\bullet}$ formation energies at the $E_{f,eq}$ for the different compositions. The gray beam is a visual reference for comparing the energies of (a,b).

by unit cell volume, can be indirectly insightful in terms of Li^+ transport. The activation energy is found to decrease for higher Li^+ carrier densities (Figure 11).

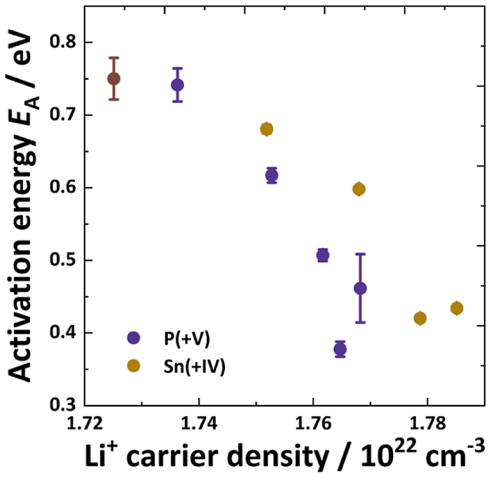

Figure 11. Correlation between Li^+ carrier density, estimated from the number of Li^+ in the unit cell and the unit cell volume, and activation energy showing a decrease of migration barrier upon increase in Li^+ carrier density.

As the energy landscape on which the Li^+ distribute and move on is normally created by the anionic framework and its modulation is related to changes in the host-framework, the connection of activation energy and Li^+ carrier density does not seem to be straightforward. However, the overall activation energy consists of the migration energy E_m and the defect formation energy ΔH_f.

$$E_A = E_m + \frac{\Delta H_f}{2}$$

The migration energy E_m is essentially the energy to move a Li^+ to another crystal site while the ΔH_f takes into account formation to create a defect. In both substitution series, the activation energy is strongly reduced and Li^+ transport significantly improved. On the one hand, the introduction of Sn(+IV) and P(+V) should modify the energy landscape and in the best case result in the occupancy of more Li^+ sites to obtain a more extensive and disordered Li^+ substructure. Nevertheless, this is not observed in this study. On the other hand, the starting material Li_3SbS_4 has an ionic conductivity of $9.2(7) \times 10^{-11}$ $S{\cdot}cm^{-1}$ at room temperature, being basically non-Li^+ conducting. The latter enforces the formation of defects for ion conduction. This might be simplified by having a higher Li^+ density in the unit cell. Statistically, the more Li^+ in the structure the higher the probability of forming a defect.

The number of defects are clearly linked to the synthesis procedure (and conditions) and composition of the materials.[54,61] As all compositions are synthesized similarly, the thermally generated defects should be comparable, hence the change in defect formation energy is more likely related to the altered composition as the defect formation energy is a function of the lithium chemical potential.[54,62] After all, the defect formation energy might be the strongest influence as these systems are not superionic conductors. Thus, the defect formation energy cannot be neglected anymore as charge carrier are not readily available and have to be created first.[63,64]

4. CONCLUSION

In this work, the substitution series $Li_{3+x}Sb_{1-x}Sn_xS_4$ and $Li_3Sb_{1-x}P_xS_4$ were synthesized and the influence of the substitutions on the structure and transport was investigated. The solubility limit seems to be influenced by geometric restrictions (P(+V)) and by the preference for the β-polymorph (Sn(+IV)). The geometric changes for Sn(+IV) are negligible, while P(+V) shows slightly more pronounced polyhedron and unit cell volume changes, however, no strong trends were observable. Both substitution series promote ionic transport of Li_3SbS_4 significantly by up to 4 orders of magnitude. Neither can be related to a better connection in the Li^+ substructure or an opening of a diffusion bottleneck. A 3-fold faster increase of Li-ion transport for $Li_{3+x}Sb_{1-x}Sn_xS_4$ compared to $Li_3Sb_{1-x}P_xS_4$ appeared puzzling as geometrical influences on Li^+ transport can be eliminated. Overall, the Li^+ carrier density might indirectly reflect changes in defect formation energy. The calculated defect formation energies depend on the chemical composition and are decreased upon the substitution of Sn(+IV) and P(+V). This work shows that the defect formation energy can influence the Li^+ transport

https://doi.org/10.1021/acsaem.3c02652
ACS Appl. Energy Mater. XXXX, XXX, XXX−XXX

strongly and cannot be neglected in the case of the investigated thio-LISICON substitutions series. Additionally, it emphasizes that the choice and combination of elements are a decisive factor on the ionic conductivity by determining the magnitude of defect formation energy.

■ ASSOCIATED CONTENT

Supporting Information

The Supporting Information is available free of charge at https://pubs.acs.org/doi/10.1021/acsaem.3c02652.

XRD data, neutron diffraction data, Rietveld refinement results, temperature-dependent impedance data, and pellet geometries and ^{6}Li MAS NMR data on $Li_{3.2}Sn_{0.8}Sb_{0.2}S_4$ and Li_4SnS_4 (PDF)

■ AUTHOR INFORMATION

Corresponding Author

Wolfgang G. Zeier − *Institute of Inorganic and Analytical Chemistry, University of Muenster, Muenster D-48149, Germany; Helmholtz Institute Muenster, FZ Jülich, Muenster D-48149, Germany;* orcid.org/0000-0001-7749-5089; Email: wzeier@uni-muenster.de

Authors

Bianca Helm − *Institute of Inorganic and Analytical Chemistry, University of Muenster, Muenster D-48149, Germany*

Kyra Strotmann − *Institute of Inorganic and Analytical Chemistry, University of Muenster, Muenster D-48149, Germany*

Thorben Böger − *Institute of Inorganic and Analytical Chemistry, University of Muenster, Muenster D-48149, Germany; International Graduate School for Battery Chemistry, Characterization, Analysis, Recycling and Application (BACCARA), University of Muenster, Muenster D-48149, Germany*

Bibek Samanta − *International Graduate School for Battery Chemistry, Characterization, Analysis, Recycling and Application (BACCARA), University of Muenster, Muenster D-48149, Germany; Institute of Physical Chemistry, University of Münster, Münster D-48149, Germany*

Ananya Banik − *Research Institute for Sustainable Energy (RISE), TCG Centre for Research and Education in Science and Technology (TCG-CREST), Kolkata 700091, India;* orcid.org/0000-0003-0455-3051

Martin A. Lange − *Institute of Inorganic and Analytical Chemistry, University of Muenster, Muenster D-48149, Germany*

Yuheng Li − *Department of Chemical and Biomolecular Engineering, National University of Singapore, Singapore 117585, Singapore; Department of Materials Science and Engineering, National University of Singapore, Singapore 117575, Singapore;* orcid.org/0000-0002-1865-1122

Cheng Li − *Oak Ridge National Laboratory (ORNL), Oak Ridge, Tennessee 37831-6473, United States;* orcid.org/0000-0002-6546-6413

Michael Ryan Hansen − *Institute of Physical Chemistry, University of Münster, Münster D-48149, Germany;* orcid.org/0000-0001-7114-8051

Pieremanuele Canepa − *Department of Chemical and Biomolecular Engineering, National University of Singapore, Singapore 117585, Singapore; Department of Materials Science and Engineering, National University of Singapore, Singapore 117575, Singapore; Department of Electrical & Computer Engineering and Texas Center for Superconductivity, University of Houston, Houston, Texas 77204, United States;* orcid.org/0000-0002-5168-9253

Complete contact information is available at: https://pubs.acs.org/10.1021/acsaem.3c02652

Notes

The authors declare no competing financial interest.

■ ACKNOWLEDGMENTS

The research was supported by the Federal Ministry of Education and Research (BMBF) within the project FESTBATT under grant number 03XP0430F. We further acknowledge funding from the Deutsche Forschungsgemeinschaft under project number 459785385. A portion of this research used resources at the Spallation Neutron Source, a DOE Office of Science User Facility operated by the Oak Ridge National Laboratory. P.C. and Y.L. acknowledge funding from the National Research Foundation under the NRF Fellowship NRFF12-2020-0012. P.C. is thankful to the Welch Foundation for supporting his Robert A. Welch professorship. T.B. and B.S. are members of the International Graduate School for Battery Chemistry, Characterization, Analysis, Recycling and Application (BACCARA), which is funded by the Ministry for Culture and Science of North Rhine Westphalia, Germany. The authors acknowledge access to "Paralleles Linux-System für Münsteraner Anwender II" (PALMA II) for DFT calculations.

■ REFERENCES

(1) Janek, J.; Zeier, W. G. A Solid Future for Battery Development. *Nat. Energy* **2016**, *1* (9), 16141.

(2) Janek, J.; Zeier, W. G. Challenges in Speeding up Solid-State Battery Development. *Nat. Energy* **2023**, *8*, 230−240.

(3) Famprikis, T.; Canepa, P.; Dawson, J. A.; Islam, M. S.; Masquelier, C. Fundamentals of Inorganic Solid-State Electrolytes for Batteries. *Nat. Mater.* **2019**, *18* (12), 1278−1291.

(4) Ohno, S.; Banik, A.; Dewald, G. F.; Kraft, M. A.; Krauskopf, T.; Minafra, N.; Till, P.; Weiss, M.; Zeier, W. G. Materials Design of Ionic Conductors for Solid State Batteries. *Prog. Energy* **2020**, *2* (2), 022001.

(5) Kraft, M. A.; Ohno, S.; Zinkevich, T.; Koerver, R.; Culver, S. P.; Fuchs, T.; Senyshyn, A.; Indris, S.; Morgan, B. J.; Zeier, W. G. Inducing High Ionic Conductivity in the Lithium Superionic Argyrodites $Li_{6+x}P_{1-x}Ge_xS_5I$ for All-Solid-State Batteries. *J. Am. Chem. Soc.* **2018**, *140* (47), 16330−16339.

(6) Zhou, L.; Assoud, A.; Zhang, Q.; Wu, X.; Nazar, L. F. New Family of Argyrodite Thioantimonate Lithium Superionic Conductors. *J. Am. Chem. Soc.* **2019**, *141* (48), 19002−19013.

(7) Deiseroth, H.-J.; Kong, S.-T.; Eckert, H.; Vannahme, J.; Reiner, C.; Zaiß, T.; Schlosser, M. Li_6PS_5X: A Class of Crystalline Li-Rich Solids With an Unusually High Li^+ Mobility. *Angew. Chem.* **2008**, *120* (4), 767−770.

(8) Kamaya, N.; Homma, K.; Yamakawa, Y.; Hirayama, M.; Kanno, R.; Yonemura, M.; Kamiyama, T.; Kato, Y.; Hama, S.; Kawamoto, K.; Mitsui, A. A Lithium Superionic Conductor. *Nat. Mater.* **2011**, *10* (9), 682−686.

(9) Bron, P.; Dehnen, S.; Roling, B. $Li_{10}Si_{0.3}Sn_{0.7}P_2S_{12}$ - A Low-Cost and Low-Grain-Boundary-Resistance Lithium Superionic Conductor. *J. Power Sources* **2016**, *329*, 530−535.

(10) Kato, Y.; Hori, S.; Kanno, R. $Li_{10}GeP_2S_{12}$-Type Superionic Conductors: Synthesis, Structure, and Ionic Transportation. *Adv. Energy Mater.* **2020**, *10* (42), 1−25.

(11) Kuhn, A.; Gerbig, O.; Zhu, C.; Falkenberg, F.; Maier, J.; Lotsch, B. V. A New Ultrafast Superionic Li-Conductor: Ion Dynamics in $Li_{11}Si_2PS_{12}$ and Comparison with Other Tetragonal LGPS-Type Electrolytes. *Phys. Chem. Chem. Phys.* **2014**, *16* (28), 14669−14674.
(12) Li, Y.; Song, S.; Kim, H.; Nomoto, K.; Kim, H.; Sun, X.; Hori, S.; Suzuki, K.; Matsui, N.; Hirayama, M.; Mizoguchi, T.; Saito, T.; Kamiyama, T.; Kanno, R. A Lithium Superionic Conductor for Millimeter-Thick Battery Electrode. *Science* **2023**, *381*, 50−53.
(13) Schlem, R.; Banik, A.; Ohno, S.; Suard, E.; Zeier, W. G. Insights into the Lithium Sub-Structure of Superionic Conductors Li_3YCl_6 and Li_3YBr_6. *Chem. Mater.* **2021**, *33* (1), 327−337.
(14) Li, X.; Liang, J.; Adair, K. R.; Li, J.; Li, W.; Zhao, F.; Hu, Y.; Sham, T. K.; Zhang, L.; Zhao, S.; Lu, S.; Huang, H.; Li, R.; Chen, N.; Sun, X. Origin of Superionic $Li_3Y_{1-x}In_xCl_6$ Halide Solid Electrolytes with High Humidity Tolerance. *Nano Lett.* **2020**, *20* (6), 4384−4392.
(15) van der Maas, E.; Zhao, W.; Cheng, Z.; Famprikis, T.; Thijs, M.; Parnell, S. R.; Ganapathy, S.; Wagemaker, M. Investigation of Structure, Ionic Conductivity, and Electrochemical Stability of Halogen Substitution in Solid-State Ion Conductor $Li_3YBr_xCl_{6-X}$. *J. Phys. Chem. C* **2023**, *127*, 125−132.
(16) Minafra, N.; Hogrefe, K.; Barbon, F.; Helm, B.; Li, C.; Wilkening, H. M. R.; Zeier, W. G. Two-Dimensional Substitution: Toward a Better Understanding of the Structure-Transport Correlations in the Li-Superionic Thio-LISICONs. *Chem. Mater.* **2021**, *33* (2), 727−740.
(17) Ramos, E. P.; Bazak, J. D.; Assoud, A.; Huq, A.; Goward, G.; Nazar, L. F. Structure of the Solid-State Electrolyte $Li_{3+2x}P_{1-x}Al_xS_4$: Lithium-Ion Transport Properties in Crystalline vs Glassy Phases. *ACS Appl. Mater. Interfaces* **2022**, *14* (51), 56767−56779.
(18) Murayama, M.; Kanno, R.; Kawamoto, Y.; Kamiyama, T. Structure of the Thio-LISICON Li_4GeS_4. *Solid State Ionics* **2002**, *154*−*155*, 789−794.
(19) Hori, S.; Kato, M.; Suzuki, K.; Hirayama, M.; Kato, Y.; Kanno, R. Phase Diagram of the Li_4GeS_4-Li_3PS_4 Quasi-Binary System Containing the Superionic Conductor $Li_{10}GeP_2S_{12}$. *J. Am. Ceram. Soc.* **2015**, *98* (10), 3352−3360.
(20) Homma, K.; Yonemura, M.; Nagao, M.; Hirayama, M.; Kanno, R. Crystal Structure of High-Temperature Phase of Lithium Ionic Conductor, Li_3PS_4. *J. Phys. Soc. Jpn.* **2010**, *79*, 90−93.
(21) Homma, K.; Yonemura, M.; Kobayashi, T.; Nagao, M.; Hirayama, M.; Kanno, R. Crystal Structure and Phase Transitions of the Lithium Ionic Conductor Li_3PS_4. *Solid State Ionics* **2011**, *182* (1), 53−58.
(22) Kaup, K.; Zhou, L.; Huq, A.; Nazar, L. F. Impact of the Li Substructure on the Diffusion Pathways in Alpha and Beta Li_3PS_4 : An in Situ High Temperature Neutron Diffraction Study. *J. Mater. Chem. A* **2020**, *8* (25), 12446−12456.
(23) Kimura, T.; Inaoka, T.; Izawa, R.; Nakano, T.; Hotehama, C.; Sakuda, A.; Tatsumisago, M.; Hayashi, A. Stabilizing High-Temperature α-Li_3PS_4 by Rapidly Heating the Glass. *J. Am. Chem. Soc.* **2023**, *145* (26), 14466−14474.
(24) Forrester, F. N.; Quirk, J. A.; Famprikis, T.; Dawson, J. A. Disentangling Cation and Anion Dynamics in Li_3PS_4 Solid Electrolytes. *Chem. Mater.* **2022**, *34* (23), 10561−10571.
(25) Liu, Z.; Fu, W.; Payzant, E. A.; Yu, X.; Wu, Z.; Dudney, N. J.; Kiggans, J.; Hong, K.; Rondinone, A. J.; Liang, C. Anomalous High Ionic Conductivity of Nanoporous β-Li_3PS_4. *J. Am. Chem. Soc.* **2013**, *135* (3), 975−978.
(26) Sahu, G.; Rangasamy, E.; Li, J.; Chen, Y.; An, K.; Dudney, N.; Liang, C. A High-Conduction Ge Substituted Li_3AsS_4 Solid Electrolyte with Exceptional Low Activation Energy. *J. Mater. Chem. A* **2014**, *2* (27), 10396−10403.
(27) Kimura, T.; Kato, A.; Hotehama, C.; Sakuda, A.; Hayashi, A.; Tatsumisago, M. Preparation and Characterization of Lithium Ion Conductive Li_3SbS_4 Glass and Glass-Ceramic Electrolytes. *Solid State Ionics* **2019**, *333*, 45−49.
(28) Giorgi, C. D. *Lithiumionenleiter - Synthese, Strukturchemie Und Leitfähigkeitsmessungen Kristalliner Lithiumverbindungen*; Universität Regensburg, 2019.
(29) Al-Qawasmeh, A.; Holzwarth, N. A. W. Computational Study of Li Ion Electrolytes Composed of Li_3AsS_4 Alloyed with Li_4GeS_4. *J. Electrochem. Soc.* **2016**, *163* (9), A2079−A2088.
(30) Yang, Y.; Wu, Q.; Cui, Y.; Chen, Y.; Shi, S.; Wang, R.-Z.; Yan, H. Elastic Properties, Defect Thermodynamics, Electrochemical Window, Phase Stability, and Li^+ Mobility of Li_3PS_4 : Insights from First-Principles Calculations. *ACS Appl. Mater. Interfaces* **2016**, *8* (38), 25229−25242.
(31) Helm, B.; Minafra, N.; Wankmiller, B.; Agne, M. T.; Li, C.; Senyshyn, A.; Hansen, M. R.; Zeier, W. G. Correlating Structural Disorder to Li^+ Ion Transport in $Li_{4-x}Ge_{1-x}Sb_xS_4$ ($0 \le x \le 0.2$). *Chem. Mater.* **2022**, *34* (12), 5558−5570.
(32) Coelho, A. A. *TOPAS-academic*: Brisbane, 2007.
(33) Huq, A.; Kirkham, M.; Peterson, P. F.; Hodges, J. P.; Whitfield, P. S.; Page, K.; Hűgle, T.; Iverson, E. B.; Parizzi, A.; Rennich, G. POWGEN: Rebuild of a Third-Generation Powder Diffractometer at the Spallation Neutron Source. *J. Appl. Crystallogr.* **2019**, *52* (5), 1189−1201.
(34) Thompson, P.; Cox, D. E.; Hastings, J. B. Rietveld Refinement of Debye-Scherrer Synchrotron X-Ray Data from Al_2O_3. *J. Appl. Crystallogr.* **1987**, *20* (2), 79−83.
(35) Momma, K.; Izumi, F. VESTA 3 for Three-Dimensional Visualization of Crystal, Volumetric and Morphology Data. *J. Appl. Crystallogr.* **2011**, *44* (6), 1272−1276.
(36) Kresse, G.; Furthmüller, J. Efficient Iterative Schemes for Ab Initio Total-Energy Calculations Using a Plane-Wave Basis Set. *Phys. Rev. B: Condens. Matter Mater. Phys.* **1996**, *54* (16), 11169−11186.
(37) Kresse, G.; Furthmüller, J. Efficiency of Ab-Initio Total Energy Calculations for Metals and Semiconductors Using a Plane-Wave Basis Set. *Comput. Mater. Sci.* **1996**, *6* (1), 15−50.
(38) Kresse, G.; Hafner, J. Ab Initio Molecular Dynamics for Liquid Metals. *Phys. Rev. B* **1993**, *47* (1), 558−561.
(39) Perdew, J. P.; Burke, K.; Ernzerhof, M. Generalized Gradient Approximation Made Simple. *Phys. Rev. Lett.* **1996**, *77* (18), 3865−3868.
(40) Kresse, G.; Joubert, D. From Ultrasoft Pseudopotentials to the Projector Augmented-Wave Method. *Phys. Rev. B* **1999**, *59* (3), 1758−1775.
(41) Broberg, D.; Medasani, B.; Zimmermann, N. E. R.; Yu, G.; Canning, A.; Haranczyk, M.; Asta, M.; Hautier, G. PyCDT: A Python Toolkit for Modeling Point Defects in Semiconductors and Insulators. *Comput. Phys. Commun.* **2018**, *226*, 165−179.
(42) Krukau, A. V.; Vydrov, O. A.; Izmaylov, A. F.; Scuseria, G. E. Influence of the Exchange Screening Parameter on the Performance of Screened Hybrid Functionals. *J. Chem. Phys.* **2006**, *125*, 224106.
(43) Freysoldt, C.; Grabowski, B.; Hickel, T.; Neugebauer, J.; Kresse, G.; Janotti, A.; Van De Walle, C. G. First-Principles Calculations for Point Defects in Solids. *Rev. Mod. Phys.* **2014**, *86* (1), 253−305.
(44) Shannon, R. D. Revised Effective Ionic Radii and Systematic Studies of Interatomic Distances in Halides and Chalcogenides. *Acta Crystallogr.* **1976**, *32* (5), 751−767.
(45) Till, P.; Agne, M. T.; Kraft, M. A.; Courty, M.; Famprikis, T.; Ghidiu, M.; Krauskopf, T.; Masquelier, C.; Zeier, W. G. Two-Dimensional Substitution Series $Na_3P_{1-x}Sb_xPS_{4-y}Se_y$ - Beyond Static Description of Structural Bottlenecks for Na^+ Transport. *Chem. Mater.* **2022**, *34* (5), 2410−2421.
(46) Culver, S. P.; Squires, A. G.; Minafra, N.; Armstrong, C. W. F.; Krauskopf, T.; Böcher, F.; Li, C.; Morgan, B. J.; Zeier, W. G. Evidence for a Solid-Electrolyte Inductive Effect in the Superionic Conductor $Li_{10}Ge_{1-x}Sn_xP_2S_{12}$. *J. Am. Chem. Soc.* **2020**, *142* (50), 21210−21219.
(47) Bron, P.; Johansson, S.; Zick, K.; Schmedt auf der Günne, J.; Dehnen, S.; Roling, B. $Li_{10}SnP_2S_{12}$: An Affordable Lithium Superionic Conductor. *J. Am. Chem. Soc.* **2013**, *135* (42), 15694−15697.
(48) Fuchs, T.; Culver, S. P.; Till, P.; Zeier, W. G. Defect-Mediated Conductivity Enhancements in $Na_{3-x}Pn_{1-x}W_xS_4$ (Pn = P, Sb) Using Aliovalent Substitutions. *ACS Energy Lett.* **2020**, *5* (1), 146−151.

https://doi.org/10.1021/acsaem.3c02652
ACS Appl. Energy Mater. XXXX, XXX, XXX−XXX

(49) Irvine, J. T. S.; Sinclair, D. C.; West, A. R. Electroceramics: Characterization by Impedance Spectroscopy. *Adv. Mater.* **1990**, *2* (3), 132−138.
(50) Brug, G. J.; van den Eeden, A. L. G.; Sluyters-Rehbach, M.; Sluyters, J. H. The Analysis of Electrode Impedances Complicated by the Presence of a Constant Phase Element. *J. Electroanal. Chem.* **1984**, *176*, 275−295.
(51) Matsuda, R.; Muto, H.; Matsuda, A. Air-Stable Li_3SbS_4 -LiI Electrolytes Synthesized via an Aqueous Ion-Exchange Process and the Unique Temperature Dependence of Conductivity. *ACS Appl. Mater. Interfaces* **2022**, *14* (46), 52440−52447.
(52) Huber, S. *Lithiumionenleiter - Strukturelle Und Impedanzspektroskopische Untersuchungen an Neuartigen Lithiumfeststoffelektrolyten*; Universität Regensburg, 2015.
(53) Ohno, S.; Bernges, T.; Buchheim, J.; Duchardt, M.; Hatz, A. K.; Kraft, M. A.; Kwak, H.; Santhosha, A. L.; Liu, Z.; Minafra, N.; Tsuji, F.; Sakuda, A.; Schlem, R.; Xiong, S.; Zhang, Z.; Adelhelm, P.; Chen, H.; Hayashi, A.; Jung, Y. S.; Lotsch, B. V.; Roling, B.; Vargas-Barbosa, N. M.; Zeier, W. G. How Certain Are the Reported Ionic Conductivities of Thiophosphate-Based Solid Electrolytes? An Interlaboratory Study. *ACS Energy Lett.* **2020**, *5* (3), 910−915.
(54) Gorai, P.; Famprikis, T.; Singh, B.; Stevanović, V.; Canepa, P. Devil Is in the Defects: Electronic Conductivity in Solid Electrolytes. *Chem. Mater.* **2021**, *33* (18), 7484−7498.
(55) Tachez, M.; Malugani, J. P.; Mercier, R.; Robert, G. Ionic Conductivity of and Phase Transition in Lithium Thiophosphate Li_3PS_4. *Solid State Ionics* **1984**, *14* (3), 181−185.
(56) Zhang, Z.; Zhang, J.; Sun, Y.; Jia, H.; Peng, L.; Zhang, Y.; Xie, J. $Li_{4-x}Sb_xSn_{1-x}S_4$ Solid Solutions for Air-Stable Solid Electrolytes. *J. Energy Chem.* **2020**, *41*, 171−176.
(57) Kwak, H.; Park, K. H.; Han, D.; Nam, K. W.; Kim, H.; Jung, Y. S. Li^+ Conduction in Air-Stable Sb-Substituted Li_4SnS_4 for All-Solid-State Li-Ion Batteries. *J. Power Sources* **2020**, *446*, 227338.
(58) Minafra, N.; Culver, S. P.; Li, C.; Senyshyn, A.; Zeier, W. G. Influence of the Lithium Substructure on the Diffusion Pathways and Transport Properties of the Thio-LISICON $Li_4Ge_{1-x}Sn_xS_4$. *Chem. Mater.* **2019**, *31* (10), 3794−3802.
(59) Kaib, T.; Haddadpour, S.; Kapitein, M.; Bron, P.; Schröder, C.; Eckert, H.; Roling, B.; Dehnen, S. New Lithium Chalcogenidotetrelates, LiChT: Synthesis and Characterization of the Li^+-Conducting Tetralithium Ortho-Sulfidostannate Li_4SnS_4. *Chem. Mater.* **2012**, *24* (11), 2211−2219.
(60) Lepley, N. D.; Holzwarth, N. A. W.; Du, Y. A. Structures, Li^+ Mobilities, and Interfacial Properties of Solid Electrolytes Li_3PS_4 and Li_3PO_4 from First Principles. *Phys. Rev. B* **2013**, *88* (10), 104103−104123.
(61) Gautam, A.; Sadowski, M.; Prinz, N.; Eickhoff, H.; Minafra, N.; Ghidiu, M.; Culver, S. P.; Albe, K.; Fässler, T. F.; Zobel, M.; Zeier, W. G. Rapid Crystallization and Kinetic Freezing of Site-Disorder in the Lithium Superionic Argyrodite Li_6PS_5Br. *Chem. Mater.* **2019**, *31* (24), 10178−10185.
(62) Combs, S. R.; Todd, P. K.; Gorai, P.; Maughan, A. E. Editors' Choice—Review—Designing Defects and Diffusion through Substitutions in Metal Halide Solid Electrolytes. *J. Electrochem. Soc.* **2022**, *169* (4), 040551.
(63) Tilley, R. J. D. *Defects in Solids*; Wiley: Chichester, UK, 2005.
(64) Dietrich, C.; Sadowski, M.; Sicolo, S.; Weber, D. A.; Sedlmaier, S. J.; Weldert, K. S.; Indris, S.; Albe, K.; Janek, J.; Zeier, W. G. Local Structural Investigations, Defect Formation, and Ionic Conductivity of the Lithium Ionic Conductor $Li_4P_2S_6$. *Chem. Mater.* **2016**, *28* (23), 8764−8773.

https://doi.org/10.1021/acsaem.3c02652
ACS Appl. Energy Mater. XXXX, XXX, XXX−XXX